66 (2021) APPLICATIONS OF MATHEMATICS No. 2, 183–211

AN XFEM/DG APPROACH FOR FLUID-STRUCTURE INTERACTION PROBLEMS WITH CONTACT

Luca Formaggia, Federico Gatti, Stefano Zonca, Milano

Received November 19, 2019. Published online January 26, 2021.

Abstract. In this work, we address the problem of fluid-structure interaction (FSI) with moving structures that may come into contact. We propose a penalization contact algorithm implemented in an unfitted numerical framework designed to treat large displacements. In the proposed method, the fluid mesh is fixed and the structure meshes are superimposed to it without any constraint on the conformity. Thanks to the Extended Finite Element Method (XFEM), we can treat discontinuities of the fluid solution on the mesh elements intersecting the structure. The coupling conditions at the fluid-structure interface are enforced via a discontinuous Galerkin mortaring technique, which is a penalization method that ensures the consistency of the scheme with the underlining problem. Concerning the contact problem, we consider a frictionless contact model in a master/slave approach. By considering the coupled FSI-contact problem, we perform some numerical tests to assess the sensitivity of the proposed method with respect to the discretization and contact parameters and we show some examples in the case of contact between a flexible body and a rigid wall and between two deformable structures.

Keywords: fluid-structure interaction; contact; extended finite element method; discontinuous Galerkin; Nitsche's method

MSC 2020: 65N30, 76M10, 74F10

1. Introduction

Many engineering applications involve the interaction between a fluid and moving structures, see e.g. [31], [62], [54], [10], [9], [61]. The numerical simulation of such phenomena is very challenging, since the structures are subject to large displacements

The authors gratefully acknowledge the financial support of the Italian MIUR by the grant PRIN12, number 201289A4LX, "Mathematical and numerical models of the cardiovascular system, and their clinical applications". S. Zonca has been supported by "GNCS-INdAM".

DOI: 10.21136/AM.2021.0310-19

and deformations and special numerical methods are required to handle the movement of the computational grids. Some applications involve the interaction between structures that may come into contact, see e.g. [51], [45], [44], [49]. A well-established approach to deal with the fluid-structure interaction (FSI) problem is the Arbitrary Lagrangian Eulerian approach (ALE), see e.g. [30], [41], [32]. Its basic idea is to introduce a new reference framework for the fluid domain that follows the movement of the boundary induced by the displacement of the structures. At the discrete level, this permits the fluid mesh to deform in accordance with the structures maintaining its conformity with the interface. However, when the displacements are too large, this approach may fail, since inverted fluid elements may appear, or may lead to an inaccurate solution due to the presence of very stretched fluid elements. The same argument can be applied when two structures approach each other. A possible remedy is to remesh or to locally adapt the fluid mesh, see e.g. [58], [8]. An alternative is to use the so-called unfitted methods. Unfitted methods rely on a fixed background grid for the fluid, while the structural elements are overlapped to it without any constraint and they are able to move independently from the fluid mesh. This class of methods includes, for example, the Immersed Boundary method [51], [52], [47], [12], [14], [16], [38], [15], the Fictitious Domain method [37], [50], [7], [13], the Fully-Eulerian approach [57], [53], [55], [35], the Extended Finite Element method (XFEM) [36], [20], [4], [64], [59], the Cut-Finite Element method [46], the Polygonal Discontinuous Galerkin method [5]. Hybrid approaches that combine the ALE method and the unfitted technology have been proposed, see e.g. [40], [19], where the ALE approach is used for dealing with the movement of the structure and the Nitsche's approach allows to weakly couple the fluid and solid at the interface.

Regarding the contact problem, several models have been proposed in the context of pure contact mechanics, see e.g. [42], [60]. A possible simple model describes the contact via the Karush-Kuhn-Tucker conditions

$$\Delta \geqslant 0, \quad \lambda \leqslant 0, \quad \lambda\Delta = 0,$$

where Δ is the distance between structures and λ is the normal traction at the structure interface. It requires to introduce variational inequalities and the resulting constraints can be imposed, for instance, via a penalization approach, see e.g. [27]. Recent works use an augmented Lagrangian/Nitsche's approach to include the contact in the discrete formulation, which is a penalization approach with the advantage that it leads to a consistent formulation, see e.g. [26], [25], [28], [29], [23], [24]. However, only few results have been proposed regarding the contact in the fluid-structure interaction framework, see e.g. [34], [21], [1], [2]. In the present work we employ the XFEM [48], [11], [39] in combination with the discontinuous Galerkin (DG) mortaring [6], [18] to discretize a FSI problem with contact. The XFEM is based on the

classical Finite Element Method (FEM) with the advantage of enriching the numerical approximation on the fluid elements crossed by the structure. In particular, it allows to treat discontinuities within an element and, for example, to represent jumps in the numerical solution. The DG approach allows to couple the fluid and structure problems at the unfitted interface, where we prescribe no-slip coupling conditions. To handle the contact between the immersed structures, we employ a penalization method that prescribes the non-penetration condition at the solid-solid interface. Notice that in [21], the authors have presented a consistent Nitsche's method for the contact model, resulting in a full Nitsche's approach for the treatment of both the FSI coupling terms and the contact one. Moreover, they formulate the FSI-contact problem in two different ways, namely, by considering either no-slip or slip coupling conditions at the fluid-structure interface. Though in our work we consider only a penalty approach for the contact model and no-slip conditions for the FSI coupling, we present some extensions in the numerical tests, in particular:

(i) the employment of unfitted meshes;
(ii) a non-linear equation for the fluid and a non-linear constitutive law for the solid;
(iii) the two-bodies contact case.

The aim of this work is to illustrate the XFEM/DG procedure and present some preliminary results in the context of FSI problem with contact. In Section 2, we introduce the fluid-structure interaction model and its XFEM/DG formulation; in Section 3, we present the contact model and the discrete approximation in the XFEM/DG framework; in Section 4, we show some numerical test cases; finally in Section 5, we draw the conclusions and discuss possible future developments.

2. Unfitted approach for fluid-structure interaction

In this section, we introduce the governing equations for the fluid-structure interaction problem and its discretization in the XFEM/DG formulation.

2.1. Fluid-structure interaction model. We consider the fluid and solid domains $\Omega^f(t)$ and $\Omega^s(t)$ and we partition their boundaries $\partial\Omega^f(t)$ and $\partial\Omega^s(t)$, equipped with the outward unit normal $\mathbf{n}^f(t)$ and $\mathbf{n}^s(t)$, as $\partial\Omega^f(t) = \Sigma(t) \cup \Gamma^f$ and $\partial\Omega^s(t) = \Sigma(t) \cup \Gamma^s$, where $\Sigma(t) = \overline{\Omega}^f(t) \cap \overline{\Omega}^s(t)$ is the fluid-structure interface with the time dependent unit normal $\mathbf{n}(t) = \mathbf{n}^s(t) = -\mathbf{n}^f(t)$, and Γ^f and Γ^s are the portions of the boundaries fixed in time, see Figure 1. Moreover, we denote $\Omega = \Omega^f(t) \cup \Omega^s(t)$.

The FSI problem in d-dimensions (with $d = 2, 3$) reads as follows:

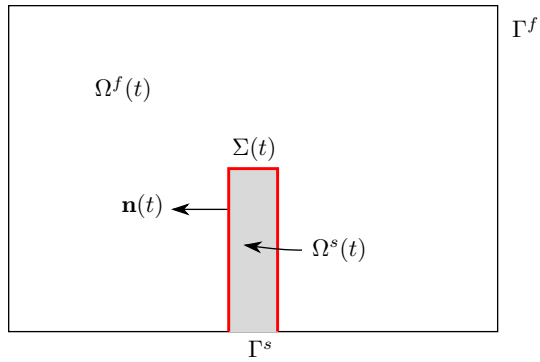

Figure 1. Sketch of the fluid and structure domains $\Omega^f(t)$ (white) and $\Omega^s(t)$ (grey) with the fluid-structure interface $\Sigma(t)$ (red).

Find, for any $t \in (0, T]$, the fluid velocity $\mathbf{u}(t)\colon\ \Omega^f(t) \to \mathbb{R}^d$, the fluid pressure $p(t)\colon\ \Omega^f(t) \to \mathbb{R}$, the solid displacement $\hat{\mathbf{d}}(t)\colon\ \widehat{\Omega}^s \to \mathbb{R}^d$, such that:

$$\begin{cases} \varrho^f \partial_t \mathbf{u} + \varrho^f \mathbf{u} \cdot \nabla \mathbf{u} - \nabla \cdot \mathbf{T}^f(\mathbf{u}, p) = \mathbf{f}^f & \text{in } \Omega^f(t), \\ \nabla \cdot \mathbf{u} = 0 & \text{in } \Omega^f(t), \\ \mathbf{u} = \mathbf{0} & \text{on } \Gamma^f; \end{cases} \tag{2.1}$$

$$\begin{cases} \varrho^s \partial_{tt} \hat{\mathbf{d}} - \nabla \cdot \widehat{\mathbf{T}}^s(\hat{\mathbf{d}}) = \hat{\mathbf{f}}^s & \text{in } \widehat{\Omega}^s, \\ \hat{\mathbf{d}} = \mathbf{0} & \text{on } \widehat{\Gamma}^s; \end{cases} \tag{2.2}$$

$$\begin{cases} \mathbf{u} = \dot{\mathbf{d}} & \text{on } \Sigma(t), \\ \mathbf{T}^f(\mathbf{u}, p)\mathbf{n} = \mathbf{T}^s(\mathbf{d})\mathbf{n} & \text{on } \Sigma(t). \end{cases} \tag{2.3}$$

Notice that we consider the fluid problem (2.1) and the coupling conditions (2.3) in the Eulerian configuration, while the structure problem (2.2) is written in the Lagrangian framework. We use the $\widehat{\cdot}$ notation to indicate the Lagrangian quantities, recalling that we can pass from the reference to the current configuration with the Lagrangian map $\widehat{\mathcal{L}}(t)\colon\ \widehat{\Omega}^s \to \Omega^s(t)$ and that we can relate a function f in the current configuration with its reference counterpart as follows:

$$f(\mathbf{x}, t) = f \circ \widehat{\mathcal{L}}(t) = \hat{f}(\hat{\mathbf{x}}, t).$$

For the fluid problem (2.1), we consider the Navier-Stokes equations for an incompressible fluid with density ϱ^f and Cauchy stress tensor $\mathbf{T}^f(\mathbf{u}, p) = -p\mathbf{I} + 2\mu^f \mathbf{D}(\mathbf{u})$, where μ^f is the dynamic viscosity and

$$\mathbf{D}(\mathbf{v}) = \frac{\nabla \mathbf{v} + \nabla \mathbf{v}^\top}{2}.$$

For the solid problem (2.2), we consider the equations of elastodynamics, denoting by ϱ^s the density of the material and by $\widehat{\mathbf{T}}^s(\hat{\mathbf{d}})$ the Piola-Kirchhoff stress tensor,

linked to the Cauchy stress tensor $\mathbf{T}^s(\mathbf{d})$ by the following formula:

$$\widehat{\mathbf{T}}^s = J\mathbf{T}^s\mathbf{F}^{-\top}.$$

Here, $J = \det(\mathbf{F})$ and $\mathbf{F} = \nabla\widehat{\mathcal{L}} = \mathbf{I} + \nabla\hat{\mathbf{d}}$ is the deformation gradient. In particular, for the tests performed in Section 4 we use the Saint Venant-Kirchhoff material law, i.e.

$$\widehat{\mathbf{T}}^s = (2\mu^s\mathbf{E} + \lambda^s\mathrm{tr}(\mathbf{E})\mathbf{I})\mathbf{F}^{\top}, \tag{2.4}$$

where $\mathbf{E} = \frac{1}{2}(\mathbf{F}^{\top}\mathbf{F} - \mathbf{I})$ is the Green-Lagrange strain tensor and μ^s, λ^s are the Lamé parameters, which can be written as functions of the Young's modulus E and the Poisson's ratio ν:

$$\mu^s = \frac{E}{2(1+\nu)}, \quad \lambda^s = \frac{E\nu}{(1+\nu)(1-2\nu)}.$$

We indicate the external forces acting on the fluid and on the solid by $\mathbf{f}^f$ and $\hat{\mathbf{f}}^s$, respectively, and we apply homogeneous Dirichlet boundary conditions on Γ^f and $\widehat{\Gamma}^s$.

Finally, to close system (2.1)–(2.3), we define the initial conditions for fluid velocity, solid displacement and solid velocity:

$$\mathbf{u}(\mathbf{x},0) = \mathbf{u}^0(\mathbf{x}) \quad \text{in } \Omega^f(0),$$
$$\hat{\mathbf{d}}(\hat{\mathbf{x}},0) = \hat{\mathbf{d}}^0(\hat{\mathbf{x}}), \quad \partial_t\hat{\mathbf{d}}(\hat{\mathbf{x}},0) = \hat{\mathbf{v}}^0(\hat{\mathbf{x}}) \quad \text{in } \widehat{\Omega}^s.$$

2.2. Numerical discretization. We introduce the background mesh $\mathcal{T}_h$ that discretizes the entire domain Ω and the solid mesh $\mathcal{T}_h^s(t)$ that covers the domain $\Omega^s(t)$. The background mesh $\mathcal{T}_h$ is fitted to $\partial\Omega$ but in general not to $\Sigma(t)$. The mesh $\mathcal{T}_h^s(t)$ overlaps $\mathcal{T}_h$, as shown in Figure 2.

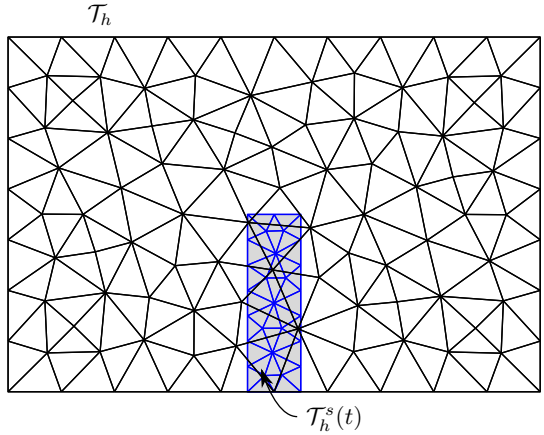

Figure 2. The structure mesh $\mathcal{T}_h^s(t)$ (grey elements with blue edges) overlaps the background mesh $\mathcal{T}_h$.

Notice that there are some elements $K \in \mathcal{T}_h$ that are partially overlapped by $\mathcal{T}_h^s(t)$, and thus split by $\Sigma(t)$ into two or more polyhedra P_K, see Figure 3. We denote these elements as *cut-elements* and we collect them in the set $\mathcal{G}_h(t)$ defined as:

$$\mathcal{G}_h(t) = \{K \in \mathcal{T}_h \colon\ K \cap \Sigma(t) \neq \emptyset\}.$$

The Extended Finite Element method allows to duplicate the set of degrees of freedom (dofs) associated with any element $K \in \mathcal{G}_h(t)$ and, for each set, to compute a numerical solution on a polyhedron P_K of the element K that belongs to the fluid domain. It is important to point out that although the background mesh $\mathcal{T}_h$ is fixed, the intersection with the foreground mesh $\mathcal{T}_h^s(t)$ changes in time due to the movement of the solid body, so the background fluid elements crossed by $\Sigma(t)$ may change from a time step to the following one. We denote by $\mathcal{F}_{\mathcal{G},h}(t)$ the set of faces F of the elements in $\mathcal{G}_h(t)$, see Figure 3. The elements $K \in \mathcal{T}_h$ completely overlapped by $\mathcal{T}_h^s(t)$ do not contribute to the numerical formulation, since they do not represent a physical portion of the domain. Further details can be found in [33], [64].

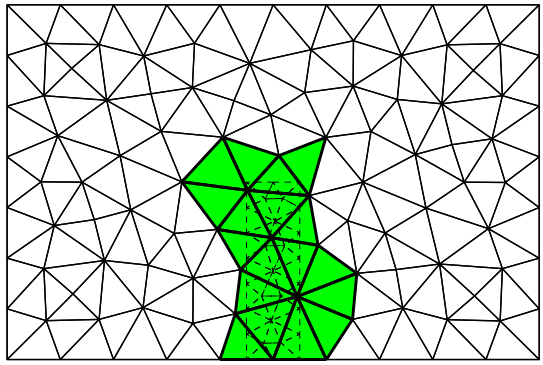

Figure 3. Representation (in green) of the set of background elements partially overlapped $\mathcal{G}_h(t)$ and the corresponding set of faces $\mathcal{F}_{\mathcal{G},h}(t)$.

The presence of cut-elements may compromise the stability of the numerical formulation. Indeed, the intersection between the background and the solid meshes may generate small polyhedral elements and hamper the conditioning of the resulting discrete formulation. A possible remedy is to introduce a stabilization term, the so-called *ghost penalty* term, see e.g. [17], which prevents the ill-conditioning of the discrete problem.

The space discretization is based on linear finite elements for the fluid velocity, pressure and solid displacement, defined as follows:

$$\mathbf{V}_h(t) = \{\mathbf{v}_h \in [X_h^f(t)]^d \colon\ \mathbf{v}_{h|\Gamma^f} = 0\}, \quad Q_h(t) = \{q_h \in X_h^f(t)\},$$
$$\widehat{\mathbf{W}}_h = \{\widehat{\mathbf{w}}_h \in [\widehat{X}_h^s]^d \colon\ \widehat{\mathbf{w}}_{h|\widehat{\Gamma}^s} = 0\},$$

where the finite element space for the fluid $X_h^f(t)$ is the direct sum of two spaces, one for the standard FEM part, i.e. for all the elements $K \notin \mathcal{G}_h(t)$, and one for the "extended" part, i.e. for all $K \in \mathcal{G}_h(t)$, namely

$$
\begin{aligned}
X_h^f(t) &= X_h^{f,\mathrm{std}}(t) \bigoplus X_h^{f,\mathrm{XFEM}}(t), \\
X_h^{f,\mathrm{std}}(t) &= \{v_h \in \mathcal{C}^0(\Omega^f(t))\colon\ v_{h|K} \in \mathbb{P}_1(K) \quad \forall\, K \in \mathcal{T}_h \setminus \mathcal{G}_h(t)\}, \\
X_h^{f,\mathrm{XFEM}}(t) &= \{v_h \in \mathcal{C}^0(\Omega^f(t))\colon\ v_{h|P_K} \in \mathbb{P}_1(P_K) \quad \forall\, P_K \in K,\ \forall\, K \in \mathcal{G}_h(t)\},
\end{aligned}
$$

while

$$
\widehat{X}_h^s = \{\widehat{w}_h \in \mathcal{C}^0(\widehat{\Omega}^s)\colon\ \widehat{w}_{h|K} \in \mathbb{P}_1(K) \quad \forall\, K \in \widehat{\mathcal{T}}_h^s\}.
$$

The proposed semi-discrete formulation of the problem described by equation (2.1)–(2.3) reads as follows:

For any $t > 0$, find $(\mathbf{u}_h(t), p_h(t), \hat{\mathbf{d}}_h(t)) \in \mathbf{V}_h(t) \times Q_h(t) \times \widehat{\mathbf{W}}_h$ such that:

$$
\begin{aligned}
(2.5) \qquad \varrho^f(\partial_t \mathbf{u}_h, \mathbf{v}_h)_{\Omega^f(t)} &+ a^f(\mathbf{u}_h, \mathbf{v}_h) + b(p_h, \mathbf{v}_h) - b(q_h, \mathbf{u}_h) \\
&+ c(\mathbf{u}_h, \mathbf{u}_h, \mathbf{v}_h) + \varrho^s(\partial_{tt}\hat{\mathbf{d}}_h, \widehat{\mathbf{w}}_h)_{\widehat{\Omega}^s} + a^s(\hat{\mathbf{d}}_h, \widehat{\mathbf{w}}_h) \\
&+ s_h(\mathbf{u}_h, p_h; \mathbf{v}_h, q_h) + g_h(\mathbf{u}_h, \mathbf{v}_h) \\
&- (\alpha \mathbf{T}^f(\mathbf{u}_h, p_h)\mathbf{n}^f + (1-\alpha)\mathbf{T}^s(\mathbf{d}_h)\mathbf{n}^f, \mathbf{v}_h - \mathbf{w}_h)_{\Sigma(t)} \\
&- (\mathbf{u}_h - \dot{\mathbf{d}}_h, \alpha \mathbf{T}^f(\mathbf{v}_h, -q_h)\mathbf{n}^f + (1-\alpha)\mathbf{T}^s(\mathbf{w}_h)\mathbf{n}^f)_{\Sigma(t)} \\
&+ \frac{\gamma_\Sigma \mu^f}{h}(\mathbf{u}_h - \dot{\mathbf{d}}_h, \mathbf{v}_h - \mathbf{w}_h)_{\Sigma(t)} \\
&= (\mathbf{f}^f, \mathbf{v}_h)_{\Omega^f(t)} + (\hat{\mathbf{f}}^s, \widehat{\mathbf{w}}_h)_{\widehat{\Omega}^s},
\end{aligned}
$$

for all $(\mathbf{v}_h(t), q_h(t), \widehat{\mathbf{w}}_h) \in \mathbf{V}_h(t) \times Q_h(t) \times \widehat{\mathbf{W}}_h$.

We have denoted

$$
\begin{aligned}
a^f(\mathbf{u}, \mathbf{v}) &= 2\mu^f(\mathbf{D}(\mathbf{u}), \nabla \mathbf{v})_{\Omega^f(t)}, \\
a^s(\hat{\mathbf{d}}, \widehat{\mathbf{w}}) &= (\widehat{\mathbf{T}}^s(\hat{\mathbf{d}}), \nabla \widehat{\mathbf{w}})_{\widehat{\Omega}_s}, \\
b(p, \mathbf{v}) &= -(p, \nabla \cdot \mathbf{v})_{\Omega^f(t)}, \\
c(\mathbf{z}, \mathbf{u}, \mathbf{v}) &= \varrho^f(\mathbf{z} \cdot \nabla \mathbf{u}, \mathbf{v})_{\Omega^f(t)},
\end{aligned}
$$

and $s_h(\mathbf{u}_h, p_h; \mathbf{v}_h, q_h)$ is the bilinear form that collects the stabilization terms for the Navier-Stokes equation and ensures the discrete inf-sup condition and the control of the velocity oscillations at high Reynolds number. In this work, the term $s_h(\mathbf{u}_h, p_h; \mathbf{v}_h, q_h)$ represents the *continuous interior penalty* stabilization, see e.g. [22]. On $\mathcal{F}_{\mathcal{G},h}(t)$ we have applied the ghost penalty stabilization term defined as

$$
g_h(\mathbf{u}_h, \mathbf{v}_h) = \gamma_g \sum_{F \in \mathcal{F}_{\mathcal{G},h}(t)} \mu^f h_F \int_F [\![\nabla \mathbf{u}_h]\!]\mathbf{n} \cdot [\![\nabla \mathbf{v}_h]\!]\mathbf{n},
$$

where $\gamma_g > 0$, $[\![\mathbf{S}]\!] = \mathbf{S}^+ - \mathbf{S}^-$ is the trace operator representing the jump of a tensor-value function $\mathbf{S}$ across the interface between the elements K^+ and K^-, while on the faces belonging to the fluid-structure interface $\Sigma(t)$ we have weakly imposed the continuity of the velocity via a Discontinuous Galerkin approach. In particular, we have employed the symmetric interior penalty method, see e.g. [6], [18], [20], with $\gamma_\Sigma > 0$ the penalty parameter and $\alpha \in [0, 1]$. We set the parameter $\alpha = 1$ to ensure numerical stability of the FSI problem, see e.g. [40], [20], [4].

Regarding the discretization in time, we employ the implicit Euler scheme for both fluid and solid problems with time step Δt. Note that the fluid integrals appearing in formulation (2.5) should be integrated on the current configuration which is itself an unknown. To handle this issue, we use a zero order extrapolation in time for the fluid domain, which coincides by taking the fluid domain at the previous time step, i.e. $\Omega^f(t^n) \approx \widetilde{\Omega}^f(t^n) = \Omega^f(t^{n-1})$.

Another issue related to the movement of the structure is how to treat the numerical solution $\mathbf{u}_h(t)$ on the fluid elements from one step to the next one. Indeed, the solution $\mathbf{u}_h(t^n)$ computed at time t^n on the domain $\widetilde{\Omega}^f(t^n)$ needs to be defined on the domain $\widetilde{\Omega}^f(t^{n+1})$ at time t^{n+1} in order to compute the right-hand term coming from the approximation formula of the time derivatives. We indicate this solution with $\widetilde{\mathbf{u}}_h(t^n)$ and to define it, we proceed as follows, depending on the geometric configuration:

(i) the fluid element K remains the same from one step to the next one, i.e. if it is fully uncovered/overlapped at time t^n, it remains fully uncovered/overlapped at time t^{n+1}. In this case, if K is uncovered, then $\widetilde{\mathbf{u}}_h(t^n)|_K = \mathbf{u}_h(t^n)|_K$, otherwise the fluid solution is not defined and thus ignored;

(ii) the uncovered portion of the fluid element K, denoted by K^+, decreases from one time step to the next one. In this case the solution is restricted on the new K^+, i.e. $\widetilde{\mathbf{u}}_h(t^n)|_{K^+(t^{n+1})} = (\mathbf{u}_h(t^n)|_{K^+(t^n)})|_{K^+(t^{n+1})}$;

(iii) the uncovered portion of the fluid element K, denoted by K^+, increases from one time step to the next one. In this case the solution is linearly extrapolated on the new K^+, i.e. $\widetilde{\mathbf{u}}_h(t^n)|_{K^+(t^{n+1})} = \mathcal{E}_{K^+(t^{n+1})}(\mathbf{u}_h(t^n)|_{K^+(t^n)})$, where $\mathcal{E}$ is an extension operator.

Further details of this procedure have been presented in [64].

The resulting fully-discrete formulation represents a non-linear system of equations which is linearized with an inexact Newton algorithm, where the fluid convective term is linearized with the Picard's method and the linearization of the solid stress tensor at the interface is approximated as follows (see [59]):

$$\frac{\partial \mathbf{T}^s}{\partial \mathbf{F}} = \frac{\partial (J^{-1} \widehat{\mathbf{T}}^s \mathbf{F}^\top)}{\partial \mathbf{F}} \approx J^{-1} \frac{\partial \widehat{\mathbf{T}}^s}{\partial \mathbf{F}} \mathbf{F}^\top.$$

3. Contact model in the unfitted framework

In this section, we consider the numerical framework presented in Section 2 in the case where both fluid-structure interaction and contact occur. We first introduce the contact model and then we consider XFEM/DG formulation for the FSI problem with contact. The contact model we present is a *master-slave* approach, i.e. the contact conditions are applied only to the *slave* body which undergoes the contact exerted by the *master* body. Moreover, we assume that the contact is frictionless, i.e. the tangential component of the contact traction is zero, by prescribing only the non-penetration condition.

3.1. Penalty contact model. To ease the presentation of the contact model, we consider two bodies described by the domains $\Omega^s(t)$ and $\Omega^m(t)$, where the *slave* body $\Omega^s(t)$ is subject to the elastodynamics equation, while the *master* body $\Omega^m(t)$ is considered rigid and fixed in time, i.e. $\Omega^m(t) = \Omega^m$. In particular, we assume that the boundary of Ω^m is modeled as a rigid plane Γ^w characterized by a given unit normal $\mathbf{n}^w$ pointing inwards Ω^m. We denote by $\mathbf{n}^s(t)$ and $\mathbf{n}^m$ the outward unit normals of $\Omega^s(t)$ and Ω^m, respectively, noticing that $\mathbf{n}^m = -\mathbf{n}^w$.

We introduce a decomposition into normal and tangential components in the frame of reference of the rigid plane Γ^w for a vector field $\mathbf{v}$ and for a stress tensor $\mathbf{T}$:

$$\mathbf{v} = v_n \mathbf{n}^w + \mathbf{v}_\mathbf{t}, \quad \mathbf{T}\mathbf{n} = T_n \mathbf{n}^w + \mathbf{T}_\mathbf{t},$$

where T_n and v_n stands for the normal components, i.e.:

$$v_n = \mathbf{v} \cdot \mathbf{n}^w, \quad T_n = \mathbf{T}\mathbf{n} \cdot \mathbf{n}^w.$$

We introduce $\Delta \colon \partial\Omega^s(t) \to \mathbb{R}$ as the *current gap* function, defined as the distance from a point $\mathbf{x}^s$ of the boundary of the slave body to the plane Γ^w, i.e. the length of the projection on the rigid plane Γ^w of any point of the current solid position, namely,

$$\Delta = (\mathbf{x}^w - \mathbf{x}^s) \cdot \mathbf{n}^w \quad \forall\, \mathbf{x}^s \in \partial\Omega^s(t),$$

where $\mathbf{x}^w$ is a generic point of Γ^w, see Figure 4. We also indicate by $\Gamma^s_C(t)$ the portion of $\partial\Omega^s(t)$ where the contact occurs.

For an elastic body the unilateral frictionless contact constraints in a master-slave approach are formulated as follows:

$$\Delta \geqslant 0, \quad \lambda \leqslant 0, \quad \lambda\Delta = 0 \quad \text{on } \partial\Omega^s(t), \tag{3.1a}$$

$$\boldsymbol{\varphi} = \mathbf{0} \quad \text{on } \partial\Omega^s(t), \tag{3.1b}$$

where $\lambda = T^s_n$ and $\boldsymbol{\varphi} = \mathbf{T}^s_\mathbf{t}$ are the normal and tangential components of the *contact traction*, respectively.

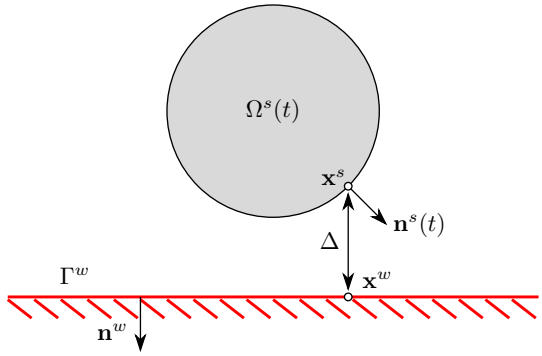

Figure 4. Sketch of the flexible body $\Omega^s(t)$ and the rigid wall Γ^w (red).

The first inequality in equation (3.1a) ensures that the solid does not cross the plane Γ^w; the second one describes that the normal component of the contact traction is zero (in absence of contact) or negative (during contact), i.e. it acts as a compression for the slave body; the third condition is the complementarity condition that guarantees that at least one of the two constraints is zero. No constraint is imposed along the tangential direction, so the contact is friction-less. Note that these conditions are the classical unilateral contact conditions (Karush-Kuhn-Tucker conditions) in the case of contact mechanics, see e.g. [42], [60], [26], [3]).

Following [27], for an arbitrary positive function γ_C defined on $\partial\Omega^s(t)$, the conditions of equation (3.1) can be approximated in a single non-linear relation

$$\lambda = -\gamma_C[-\Delta]_{\mathbb{R}^+}, \tag{3.2}$$

where the notation $[\cdot]_{\mathbb{R}^+}$ stands for the projection onto $\mathbb{R}^+$, namely,

$$[x]_{\mathbb{R}^+} = \frac{1}{2}(|x| + x) = \begin{cases} x, & x > 0, \\ 0, & x \leqslant 0. \end{cases}$$

R e m a r k 3.1. Notice that the relation given by equation (3.2) is not equivalent to the contact conditions of equation (3.1) and indeed it will yield a non-consistent formulation. In fact, a consistent formulation can be recovered replacing relation (3.2) with

$$\lambda = -\gamma_C\Big[-\Delta - \frac{1}{\gamma_C}\lambda\Big]_{\mathbb{R}^+},$$

see e.g. [26], [25], [28], [29].

In the variational setting, the contact conditions lead to the introduction of the traction λ on the boundary of the slave body. In particular, relation (3.2) leads to

the following variational penalty contact term:

$$-\int_{\partial\Omega^s(t)} \lambda w_n = +\gamma_C \int_{\partial\Omega^s(t)} [-\Delta]_{\mathbb{R}^+} w_n = -\gamma_C \int_{\Gamma_C^s(t)} \Delta w_n. \tag{3.3}$$

3.2. XFEM/DG formulation for FSI-contact model. In what follows, we consider a slave structure $\Omega^s(t)$ fully immersed in a fluid $\Omega^f(t)$ and a master structure $\Omega^m(t)$, by assuming that the slave body $\Omega^s(t)$ is subject to the elastodynamics equation while the master one $\Omega^m(t)$ is considered rigid, fixed in time and its boundary coincides with a boundary of the fluid domain indicated with Γ^w, see Figure 5. We denote by $\Sigma^s(t)$ the fluid-structure interface between the fluid and the slave body. Notice that $\Sigma^s(t) = \partial\Omega^s(t)$.

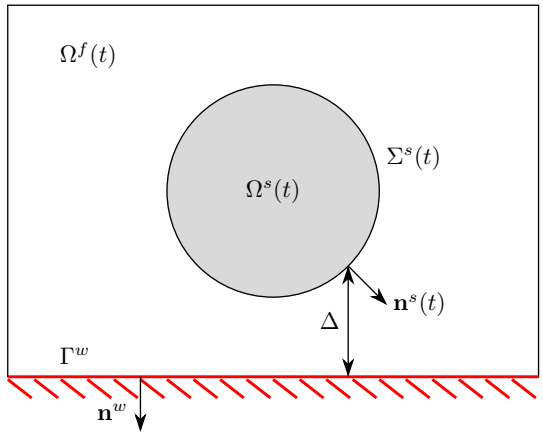

Figure 5. Sketch of the fluid and structure domains $\Omega^f(t)$ (white) and $\Omega^s(t)$ (grey) and the boundary of the master body Γ^w (red).

The coupling between the FSI problem introduced in Section 2.1 with the contact model presented in Section 3.1 leads to the following problem:

Find, for any $t \in (0, T]$, the fluid velocity $\mathbf{u}(t)\colon\ \Omega^f(t) \to \mathbb{R}^d$, the fluid pressure $p(t)\colon\ \Omega^f(t) \to \mathbb{R}$, the solid displacement $\hat{\mathbf{d}}^s(t)\colon\ \widehat{\Omega}^s \to \mathbb{R}^d$, such that:

$$\begin{cases} \varrho^f \partial_t \mathbf{u} + \varrho^f \mathbf{u} \cdot \nabla \mathbf{u} - \nabla \cdot \mathbf{T}^f(\mathbf{u}, p) = \mathbf{f}^f & \text{in } \Omega^f(t), \\ \nabla \cdot \mathbf{u} = 0 & \text{in } \Omega^f(t), \\ \mathbf{u} = \mathbf{0} & \text{on } \Gamma^f \cup \Gamma^w; \end{cases} \tag{3.4}$$

$$\varrho^s \partial_{tt} \hat{\mathbf{d}}^s - \nabla \cdot \widehat{\mathbf{T}}^s(\hat{\mathbf{d}}^s) = \hat{\mathbf{f}}^s \quad \text{in } \widehat{\Omega}^s; \tag{3.5}$$

$$\begin{cases} \mathbf{u} = \dot{\mathbf{d}}^s & \text{on } \Sigma^s(t), \\ \mathbf{T}^f(\mathbf{u}, p)\mathbf{n} = \mathbf{T}^s(\mathbf{d}^s)\mathbf{n} & \text{on } \Sigma^s(t), \\ \Delta \geqslant 0, \quad \lambda \leqslant 0, \quad \lambda\Delta = 0 & \text{on } \Sigma^s(t), \\ \boldsymbol{\varphi} = \mathbf{0} & \text{on } \Sigma^s(t). \end{cases} \tag{3.6}$$

By using the same discrete functional spaces for the approximation of the fluid velocity, fluid pressure and solid displacement introduced in Section 2.2, and by applying the penalty contact model given by equation (3.1), we write the semi-discrete formulation of the problem given by equations (3.4)–(3.6) as follows:

For any $t > 0$, find $(\mathbf{u}_h(t), p_h(t), \hat{\mathbf{d}}_h^s(t)) \in \mathbf{V}_h(t) \times Q_h(t) \times \widehat{\mathbf{W}}_h^s$ such that

$$
\begin{aligned}
(3.7)\qquad \varrho^f(\partial_t \mathbf{u}_h, \mathbf{v}_h)_{\Omega^f(t)} &+ a^f(\mathbf{u}_h, \mathbf{v}_h) + b(p_h, \mathbf{v}_h) - b(q_h, \mathbf{u}_h) \\
&+ c(\mathbf{u}_h, \mathbf{u}_h, \mathbf{v}_h) + \varrho^s(\partial_{tt}\hat{\mathbf{d}}_h^s, \widehat{\mathbf{w}}_h^s)_{\widehat{\Omega}^s} + a^s(\hat{\mathbf{d}}_h^s, \widehat{\mathbf{w}}_h^s) \\
&+ s_h(\mathbf{u}_h, p_h; \mathbf{v}_h, q_h) + g_h(\mathbf{u}_h, \mathbf{v}_h) \\
&- (\alpha \mathbf{T}^f(\mathbf{u}_h, p_h)\mathbf{n}^f + (1-\alpha)\mathbf{T}^s(\mathbf{d}_h^s)\mathbf{n}^f, \mathbf{v}_h - \mathbf{w}_h^s)_{\Sigma^s(t)} \\
&- (\mathbf{u}_h - \dot{\mathbf{d}}_h^s, \alpha \mathbf{T}^f(\mathbf{v}_h, -q_h)\mathbf{n}^f + (1-\alpha)\mathbf{T}^s(\mathbf{w}_h^s)\mathbf{n}^f)_{\Sigma^s(t)} \\
&+ \frac{\gamma_\Sigma \mu^f}{h}(\mathbf{u}_h - \dot{\mathbf{d}}_h^s, \mathbf{v}_h - \mathbf{w}_h^s)_{\Sigma^s(t)} \\
&+ \frac{\gamma_C}{h}\int_{\Sigma^s(t)} [-\Delta]_{\mathbb{R}^+} w_{n,h}^s \\
&= (\mathbf{f}^f, \mathbf{v}_h)_{\Omega^f} + (\hat{\mathbf{f}}^s, \widehat{\mathbf{w}}_h)_{\widehat{\Omega}^s}
\end{aligned}
$$

for all $(\mathbf{v}_h(t), q_h(t), \widehat{\mathbf{w}}_h) \in \mathbf{V}_h(t) \times Q_h(t) \times \widehat{\mathbf{W}}_h^s$, where $\gamma_C > 0$ is a positive penalty parameter.

Notice that the contact term in (3.7) is non null only when the argument of the projection function is positive, i.e. only when contact happens. In this case we can define a subset $\Gamma_C^s(t) \subset \partial\Omega^s(t)$ which identifies the contact surface

$$\Gamma_C^s(t) = \{\mathbf{x} \in \partial\Omega^s(t) \colon\ \Delta < 0\}.$$

R e m a r k 3.2. For practical purposes, it may be convenient to relax the contact conditions by introducing a small parameter $\varepsilon > 0$, such that we can consider that the slave body comes into contact with the master one only if the distance between them is lower than ε, i.e. $\Delta < \varepsilon$. This choice allows to avoid penetration between the bodies during the iterative procedure in the numerical solver. Hence, we can reformulate the contact condition as

$$
\begin{gathered}
\Delta - \varepsilon \geqslant 0, \quad \lambda \leqslant 0, \quad \lambda(\Delta - \varepsilon) = 0 \quad \text{on } \partial\Omega^s(t), \\
\boldsymbol{\varphi} = \mathbf{0} \quad \text{on } \partial\Omega^s(t),
\end{gathered}
$$

and the variational penalty contact term given by equation (3.3) becomes

$$-\int_{\partial\Omega^s(t)} \lambda w_n^s = +\gamma_C \int_{\partial\Omega^s(t)} [\varepsilon - \Delta]_{\mathbb{R}^+} w_n^s = +\gamma_C \int_{\Gamma_C^s(t)} (\varepsilon - \Delta) w_n^s.$$

By applying the time discretization as described in Section 2.2, the fully-discrete formulation reads as follows:

For any $n = 0, \dots, T/\Delta t - 1$, $T > 0$, find $(\mathbf{u}_h^{n+1}, p_h^{n+1}, \hat{\mathbf{d}}_h^{s,n+1}) \in \mathbf{V}_h^{n+1} \times Q_h^{n+1} \times \widehat{\mathbf{W}}_h^s$ such that

$$
\begin{aligned}
&\frac{\varrho^f}{\Delta t}(\mathbf{u}_h^{n+1}, \mathbf{v}_h)_{\Omega^{f,n}} + a^f(\mathbf{u}_h^{n+1}, \mathbf{v}_h) + b(p_h^{n+1}, \mathbf{v}_h) \\
&\qquad - b(q_h, \mathbf{u}_h^{n+1}) + c(\mathbf{u}_h^{n+1}, \mathbf{u}_h^{n+1}, \mathbf{v}_h) \\
&\qquad + \frac{\varrho^s}{\Delta t^2}(\hat{\mathbf{d}}_h^{s,n+1}, \widehat{\mathbf{w}}_h^s)_{\widehat{\Omega}^s} + a^s(\hat{\mathbf{d}}_h^{s,n+1}, \widehat{\mathbf{w}}_h^s) \\
&\qquad + s_h(\mathbf{u}_h^{n+1}, p_h^{n+1}; \mathbf{v}_h, q_h) + g_h(\mathbf{u}_h^{n+1}, \mathbf{v}_h) \\
&\qquad - (\alpha \mathbf{T}^f(\mathbf{u}_h^{n+1}, p_h^{n+1})\mathbf{n}^f + (1-\alpha)\mathbf{T}^s(\mathbf{d}_h^s)\mathbf{n}^f, \mathbf{v}_h - \mathbf{w}_h^s)_{\Sigma^{s,n}} \\
&\qquad - \Big(\mathbf{u}_h^{n+1} - \frac{\mathbf{d}_h^{s,n+1}}{\Delta t}, \alpha \mathbf{T}^f(\mathbf{v}_h, -q_h)\mathbf{n}^f + (1-\alpha)\mathbf{T}^s(\mathbf{w}_h^s)\mathbf{n}^f\Big)_{\Sigma^{s,n}} \\
&\qquad + \frac{\gamma_\Sigma \mu^f}{h}\Big(\mathbf{u}_h^{n+1} - \frac{\mathbf{d}_h^{s,n+1}}{\Delta t}, \mathbf{v}_h - \mathbf{w}_h^s\Big)_{\Sigma^{s,n}} \\
&\qquad + \frac{\gamma_C}{h}\int_{\Sigma^{s,n}} [-\Delta^{n+1}]_{\mathbb{R}^+} w_{n,h}^s \\
&= \frac{\varrho^f}{\Delta t}(\mathbf{u}_h^n, \mathbf{v}_h)_{\Omega^{f,n}} + \frac{2\varrho^s}{\Delta t^2}(\hat{\mathbf{d}}_h^{s,n}, \widehat{\mathbf{w}}_h^s)_{\widehat{\Omega}^s} - \frac{\varrho^s}{\Delta t^2}(\hat{\mathbf{d}}_h^{s,n-1}, \widehat{\mathbf{w}}_h^s)_{\widehat{\Omega}^s} \\
&\qquad + \Big(\frac{\mathbf{d}_h^{s,n}}{\Delta t}, \alpha \mathbf{T}^f(\mathbf{v}_h, -q_h)\mathbf{n}^f + (1-\alpha)\mathbf{T}^s(\mathbf{w}_h^s)\mathbf{n}^f\Big)_{\Sigma^{s,n}} \\
&\qquad - \frac{\gamma_\Sigma \mu^f}{h}\Big(\frac{\mathbf{d}_h^{s,n}}{\Delta t}, \mathbf{v}_h - \mathbf{w}_h^s\Big)_{\Sigma^{s,n}} + (\hat{\mathbf{f}}^f, \mathbf{v}_h)_{\Omega^{f,n}} + (\hat{\mathbf{f}}^s, \widehat{\mathbf{w}}_h^s)_{\widehat{\Omega}^s}
\end{aligned}
$$

for all $(\mathbf{v}_h, q_h, \widehat{\mathbf{w}}_h) \in \mathbf{V}_h^{n+1} \times Q_h^{n+1} \times \widehat{\mathbf{W}}_h^s$.

To extend the formulation presented above for the case of contact between flexible bodies, i.e. when also $\Omega^m(t)$ is subject to the elastodynamics equation, we have to generalize the definition of the current gap function Δ. First, we introduce the projection map $\Pi\colon\ \partial\Omega^s(t) \to \partial\Omega^m(t)$ that, given a point on the boundary of the slave body $\mathbf{x}^s \in \partial\Omega^s(t)$, returns its projection on the boundary of the master domain. The current gap function Δ is now given by

$$
\Delta = (\Pi(\mathbf{x}^s) - \mathbf{x}^s) \cdot \widetilde{\mathbf{n}}^w \quad \forall\, \mathbf{x}^s \in \partial\Omega^s(t),
$$

where $\widetilde{\mathbf{n}}^w$ is the unit normal pointing inwards $\Omega^m(t)$ of $\Pi(\mathbf{x}^s)$, i.e. $\widetilde{\mathbf{n}}^w = \mathbf{n}^w \circ \Pi(\mathbf{x}^s)$. Notice that, by denoting $\mathbf{x}^m = \Pi(\mathbf{x}^s)$, we have $\mathbf{n}^m(\mathbf{x}^m) = -\widetilde{\mathbf{n}}^w$.

The fully-discrete formulation in the case of two elastic bodies reads as follows:

For any $n = 0, \dots, T/\Delta t - 1$, $T > 0$, find $(\mathbf{u}_h^{n+1}, p_h^{n+1}, \hat{\mathbf{d}}_h^{s,n+1}, \hat{\mathbf{d}}_h^{m,n+1}) \in \mathbf{V}_h^{n+1} \times Q_h^{n+1} \times \widehat{\mathbf{W}}_h^s \times \widehat{\mathbf{W}}_h^m$ such that

$$
\begin{aligned}
&\frac{\varrho^f}{\Delta t}(\mathbf{u}_h^{n+1}, \mathbf{v}_h)_{\Omega^{f,n}} + a^f(\mathbf{u}_h^{n+1}, \mathbf{v}_h) + b(p_h^{n+1}, \mathbf{v}_h) - b(q_h, \mathbf{u}_h^{n+1}) \\
&\quad + c(\mathbf{u}_h^{n+1}, \mathbf{u}_h^{n+1}, \mathbf{v}_h) + \sum_{i=s,m} \Big(\frac{\varrho^i}{\Delta t^2}(\hat{\mathbf{d}}_h^{i,n+1}, \widehat{\mathbf{w}}_h^i)_{\widehat{\Omega}^i} + a^i(\hat{\mathbf{d}}_h^{i,n+1}, \widehat{\mathbf{w}}_h^i) \Big) \\
&\quad + s_h(\mathbf{u}_h^{n+1}, p_h^{n+1}; \mathbf{v}_h, q_h) + g_h(\mathbf{u}_h^{n+1}, \mathbf{v}_h) \\
&\quad - \sum_{i=s,m} (\alpha \mathbf{T}^f(\mathbf{u}_h^{n+1}, p_h^{n+1})\mathbf{n}^f + (1-\alpha)\mathbf{T}^i(\mathbf{d}_h^i)\mathbf{n}^f, \mathbf{v}_h - \mathbf{w}_h^i)_{\Sigma^{i,n}} \\
&\quad - \sum_{i=s,m} \Big(\mathbf{u}_h^{n+1} - \frac{\mathbf{d}_h^{i,n+1}}{\Delta t}, \alpha \mathbf{T}^f(\mathbf{v}_h, -q_h)\mathbf{n}^f + (1-\alpha)\mathbf{T}^i(\mathbf{w}_h^i)\mathbf{n}^f \Big)_{\Sigma^{i,n}} \\
&\quad + \sum_{i=s,m} \frac{\gamma_\Sigma \mu^f}{h} \Big(\mathbf{u}_h^{n+1} - \frac{\mathbf{d}_h^{i,n+1}}{\Delta t}, \mathbf{v}_h - \mathbf{w}_h^i \Big)_{\Sigma^{i,n}} \\
&\quad + \frac{\gamma_C}{h} \int_{\Sigma^{s,n}} [-\Delta^{n+1}]_{\mathbb{R}^+}(w_{n,h}^s - w_{n,h}^m) \\
&= \frac{\varrho^f}{\Delta t}(\mathbf{u}_h^n, \mathbf{v}_h)_{\Omega^{f,n}} + \sum_{i=s,m} \Big(\frac{2\varrho^i}{\Delta t^2}(\hat{\mathbf{d}}_h^{i,n}, \widehat{\mathbf{w}}_h^i)_{\widehat{\Omega}^i} - \frac{\varrho^i}{\Delta t^2}(\hat{\mathbf{d}}_h^{i,n-1}, \widehat{\mathbf{w}}_h^i)_{\widehat{\Omega}^i} \Big) \\
&\quad + \sum_{i=s,m} \Big(\frac{\mathbf{d}_h^{i,n}}{\Delta t}, \alpha \mathbf{T}^f(\mathbf{v}_h, -q_h)\mathbf{n}^f + (1-\alpha)\mathbf{T}^i(\mathbf{w}_h^i)\mathbf{n}^f \Big)_{\Sigma^{s,n}} \\
&\quad - \sum_{i=s,m} \frac{\gamma_\Sigma \mu^f}{h} \Big(\frac{\mathbf{d}_h^{i,n}}{\Delta t}, \mathbf{v}_h - \mathbf{w}_h^i \Big)_{\Sigma^{i,n}} + (\mathbf{f}^f, \mathbf{v}_h)_{\Omega^{f,n}} + \sum_{i=s,m} (\hat{\mathbf{f}}^i, \widehat{\mathbf{w}}_h^i)_{\widehat{\Omega}^i}
\end{aligned}
$$

for all $(\mathbf{v}_h, q_h, \widehat{\mathbf{w}}_h) \in \mathbf{V}_h^{n+1} \times Q_h^{n+1} \times \widehat{\mathbf{W}}_h^s \times \widehat{\mathbf{W}}_h^m$.

4. Numerical examples

In this section, we present four numerical examples concerning the penalty contact model for FSI presented in Section 3. For all the numerical tests, we consider an elastic ball (described by the constitutive law in equation (2.4)) immersed in a fluid that comes into contact with the ground. As a preliminary test, we check the sensibility of the proposed contact method with respect to the discretization parameters and the contact ones, see Section 4.1. Then we consider the moving elastic ball coming in contact with:

(i) a virtual barrier immersed in the fluid, see Section 4.2;
(ii) a rigid ground, see Section 4.3;
(iii) an elastic ground, see Section 4.4.

We introduce some quantities that will be used throughout the following examples: $d_{\min}(t)$ is the minimum distance between the ball and the ground at time t, respectively; $u_y(t)$ and $a_y(t)$ are the y-velocity and y-acceleration of the ball at time t; d^b is the amplitude of the bounce of the ball, i.e. the difference between the maximum height reached by the ball after the bounce and the minimum distance between the ball and the ground during the contact phase; u_y^b is the maximum y-velocity reached by the ball after the bounce; $(d_{\max} - d_{\min})(t)$ defines the compression of the ball, computed as the difference between the maximum distance between the ball and the ground and the minimum one at time t.

At each time step, we treat the non-linearities via the inexact Newton method presented in [59] and the resulting linear system is solved monolithically via the GMRES iterative solver with a block Gauss-Seidel preconditioner, see [63].

The XFEM/DG approach has been developed in the finite elements library LifeV [43]. For further details on the implementation and on some results that assess the effectiveness of the proposed XFEM/DG approach as well as a comparison of this method with respect to the ALE one in the case of FSI problem (with no contact), see [64].

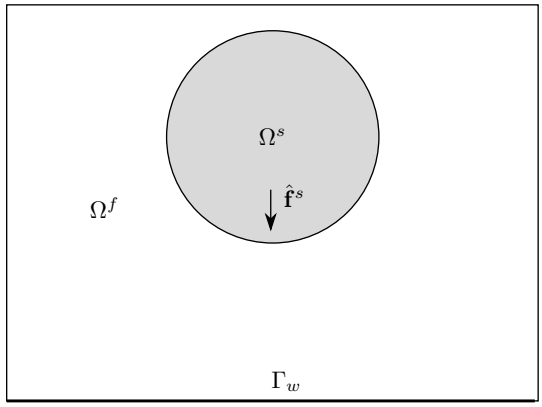

Figure 6. The ball Ω^s (grey) is immersed in the fluid domain Ω^f (white) and Γ^w is the bottom boundary of the fluid domain.

4.1. Sensitivity test on the contact model. The goal of this numerical example is to show how the choice of the discretization parameters, namely h and Δt, and the contact ones, namely γ_C and ε (see Remark 3.2), influences the dynamics of the system. We consider a background domain $\Omega = (0, 0.5)\,\text{cm} \times (0, 0.325)\,\text{cm}$ and a solid domain $\widehat{\Omega}^s$ defined by a disk of radius $0.05\,\text{cm}$ with center in $(0.25, 0.175)$. The fluid domain is then defined as $\Omega^f = \Omega \setminus \Omega^s$. The fluid represents the air with a dynamic viscosity $\mu^f = 1.81 \cdot 10^{-4}\,\text{dyne s}$ and density $\varrho^f = 1.225 \cdot 10^{-3}\,\text{g/cm}^2$. The

solid domain represents an elastic ball with density $\varrho^s = 0.1\,\mathrm{g/cm^2}$, Young's modulus $E = 10^3\,\mathrm{dyne/cm}$ and Poisson's ratio $\nu = 0.45$. The ball is subject to a force $\hat{\mathbf{f}}^s = \varrho^s \cdot (0, -10^3)\,\mathrm{cm/s^2}$ that moves the ball towards the bottom boundary of the fluid domain $\Gamma^w = \{(x, y) \in \mathbb{R}^2 \colon y = 0\}$, see Figure 6. We study the dynamics of the system by considering a final time $T = 0.03\,\mathrm{s}$.

For the numerical simulations, we set as default values
$h = 0.015\,\mathrm{cm}$, $\Delta t = 2 \cdot 10^{-4}\,\mathrm{s}$, $\varepsilon = 0.015\,\mathrm{cm}$, $\gamma_C = 10^4$, $\gamma_g = 1$ and $\gamma_\Sigma = 10^5$.

For the sensitivity analysis, we consider the following values:
$h = \{0.01, 0.015, 0.02\}\,\mathrm{cm}$, $\Delta t = \{0.5, 1, 2, 5\} \cdot 10^{-4}\,\mathrm{s}$, $\varepsilon = \{0.2, 0.5, 1, 1.5, 2\}\,h$ and $\gamma_C = \{10^3, 10^4, 10^5\}$.

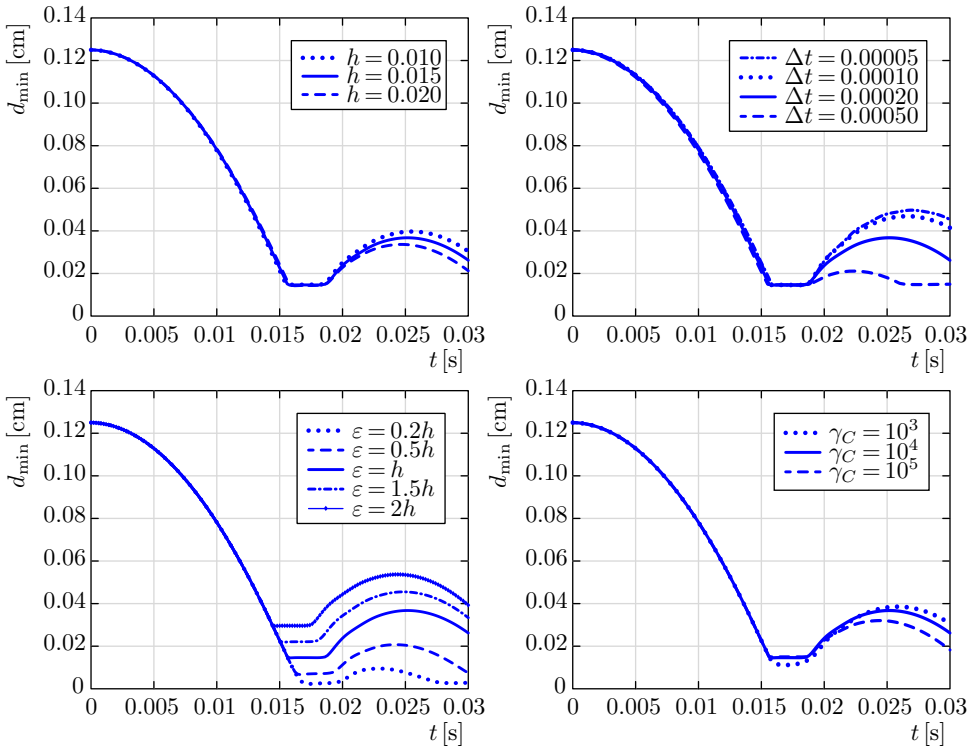

Figure 7. Minimum distance of the ball with respect to the ground as a function of time. Sensitivity with respect to: h (top-left); Δt (top-right); ε (bottom-left); γ_C (bottom-right). "Sensitivity" test case.

In Figure 7, we report the evolution of $d_{\min}$ through time for the four selected parameters. We see that different values of the spatial discretization h lead to a different dynamics of the bounce of the ball: as h decreases the maximum height reached by the ball after the bounce increases, see Figure 7 (top-left). A similar behaviour is

achieved when Δt decreases, see Figure 7 (top-right). This is an expected result, since as soon as h and Δt approach zero, the numerical dissipation is reduced. Regarding the sensibility with respect to ε, see Figure 7 (bottom-left), as far as ε tends to zero, the amplitude of the bounce d^b, as well as the maximum y-velocity reached after the rebound u_y^b, decrease, and drop sensibly when ε becomes lower than h, see Table 1 and Figure 8. Regarding the penalty constant γ_C, if it is too low, i.e. $\gamma_C = 10^3$, the non-penetration condition is violated, see Figure 7 (bottom-right). On the other hand, if γ_C is too high, i.e. $\gamma_C = 10^5$, a "sticky" effect may happen between the ball and the ground inhibiting the release from the contact phase, see Figure 7.

ε	d^b[cm]	u_y^b[cm/s]
$2h$	0.0242	7.5815
$1.5h$	0.0236	7.4215
h	0.0222	7.4335
$0.5h$	0.0140	5.5355
$0.2h$	0.0072	3.7293

Table 1. Amplitude of the bounce of the ball and its maximum y-velocity reached after the rebound for different values of ε. "Sensitivity" test case.

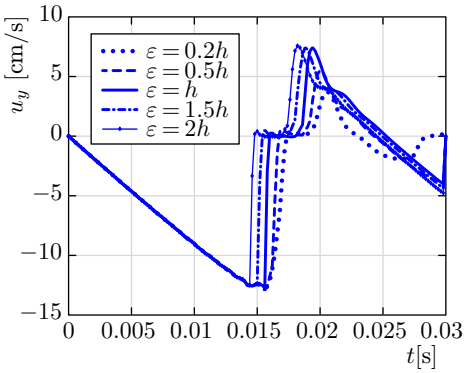

Figure 8. y-velocity of the ball for different values of ε. "Sensitivity" test case.

Finally, in Figure 9, we show the distance $d_{\min}$ when both h and ε decrease, with $h = \varepsilon$, i.e. by maintaining one layer of elements in between the ball and the ground. We can see that for decreasing values of h, the contact happens later and the release of the ball is accordingly delayed, by maintaining a similar amplitude of the bounce.

From this analysis, we found that a good choice for the contact relaxation parameter is to set $\varepsilon \approx h$, while the contact penalty parameter γ_C can be set $\approx 10^4$, though we expect that it may depend on the material properties or on the forces affecting the system.

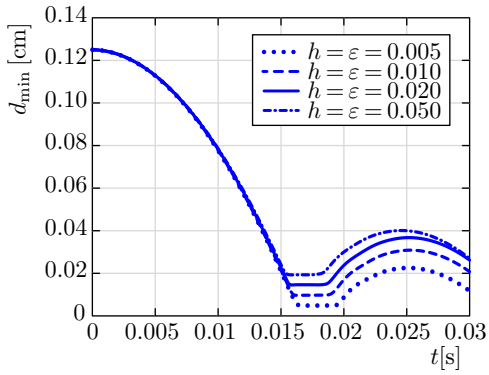

Figure 9. Minimum distance of the ball with respect to the ground as a function of time, for different values of $h = \varepsilon$. "Sensitivity" test case.

4.2. Contact of an elastic ball with a virtual barrier. To test the proposed contact algorithm implemented in the XFEM/DG method, we consider a 2D elastic ball immersed in a fluid moving towards a planar rigid ground, see Figure 6. Here, we are interested to show that the ball is subjected to a repulsive force when it reaches a specific distance from the rigid ground. To assess this without considering the geometric contact between the ball and the ground, we model the presence of a virtual barrier by setting $\varepsilon \gg 0$. We expect that the ball stops moving towards the rigid ground when it reaches the virtual barrier. The solid domain $\widehat{\Omega}^s$ is a disk of radius $4\,\mathrm{cm}$ with center located at $(0, 10)\,\mathrm{cm}$. The solid is fully immersed in a fluid domain $\Omega^f(t)$ and moves towards the boundary of the fluid domain $\Gamma^w = \{(x, y) \in \mathbb{R}^2 \colon\ y = 0\}$, due to the force $\hat{\mathbf{f}}^s = \varrho^s \cdot (0, -10^3)\,\mathrm{cm/s^2}$. We denote with $\Omega = (-10, 10)\,\mathrm{cm} \times (0, 15)\,\mathrm{cm}$ the domain given by the union of the solid and fluid domains. Moreover, to model the virtual barrier we set $\varepsilon = 3\,\mathrm{cm}$. Initially both the fluid and the solid are at rest. On the boundary Γ^w, we apply a zero velocity condition, while on the other part of the boundary fluid domain we apply a homogeneous Neumann condition.

For the physical parameters, we use the Lamé parameters $\mu^s = 2 \cdot 10^6\,\mathrm{dyne/cm}$, $\lambda^s = 8 \cdot 10^6\,\mathrm{dyne/cm}$, the fluid dynamic viscosity $\mu^f = 10^{-2}\,\mathrm{dyne\,s}$, and the fluid and solid densities $\varrho^s = \varrho^f = 1\,\mathrm{g/cm^2}$.

Due to the low Reynolds number and the symmetry of the problem, we expect to obtain a symmetric solution with respect to the vertical axis. For this reason, we decide to simulate only half of the domain to reduce the computational cost, by imposing symmetry boundary conditions on the plane of symmetry, i.e. $\hat{\mathbf{d}}^s \cdot \hat{\mathbf{n}} = 0$ and $\mathbf{u} \cdot \mathbf{n} = 0$ for the solid and fluid, respectively, see Figure 10 (left).

We use a non-uniform isotropic background mesh with a space resolution of $0.5\,\mathrm{cm}$ in the upper part of the domain and of $0.1\,\mathrm{cm}$ in the proximity of the wall Γ^w. For

the solid mesh we use a uniform isotropic grid of size 0.1 cm. In Figure 10 (right), we sketch the background and foreground meshes used in the simulations. For the numerical setting, we choose $\gamma_g = 1$, $\gamma_\Sigma = 10^5$, $\gamma_C = 10^8$ and $\Delta t = 10^{-3}$ s.

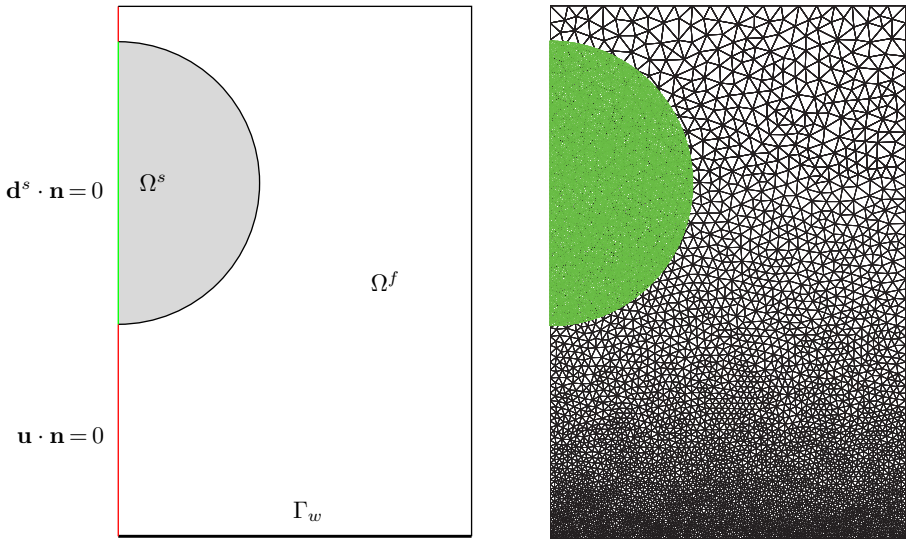

Figure 10. Sketch of the reduced domain (left) and the corresponding mesh (right). "Virtual barrier" test case.

In Figure 11, we plot the minimum distance $d_{\min}$ over time, the compression $d_{\max} - d_{\min}$ of the ball over time, the y-velocity and y-acceleration related to the point at minimum distance between the ball and Γ^w. We observe that the solid is pulled down by the body force $\hat{\mathbf{f}}^s$ until it reaches the virtual barrier at time 0.111 s.

Since the virtual barrier is non physical, the ball does not feel its presence until it touches the barrier and the contact penalty term activates. For this reason, the ball arrives in contact with the virtual barrier without any previous compression, i.e. there is not a significant increase of the pressure at the bottom of the ball. Then, at time 0.126 s, the ball is released from contact and it reaches its maximum height at time 0.182 s, i.e. $d_{\min} \approx 3.8$ cm. From this point the ball moves again towards the bottom due to body force $\hat{\mathbf{f}}^s$.

During contact, the maximum violation of the non-penetration condition below ε corresponds to about 1% of the local mesh size.

From Figure 11 (bottom-left), we observe that the compression concerning the ball during the contact phase causes the activation of some vibration modes in the structure, which are then damped. Note that the strong variations in the velocity u_y correspond to the collision and release of the ball with the virtual barrier, see Figure 11 (top-right), and the peaks in the acceleration a_y are due to the discontinuities

in the velocity, see Figure 11 (bottom-right). As stated above, since the ball does not feel the presence of the virtual barrier, it does not exhibit a significant decrease of the velocity and its acceleration remains constant until the ball touches the virtual barrier.

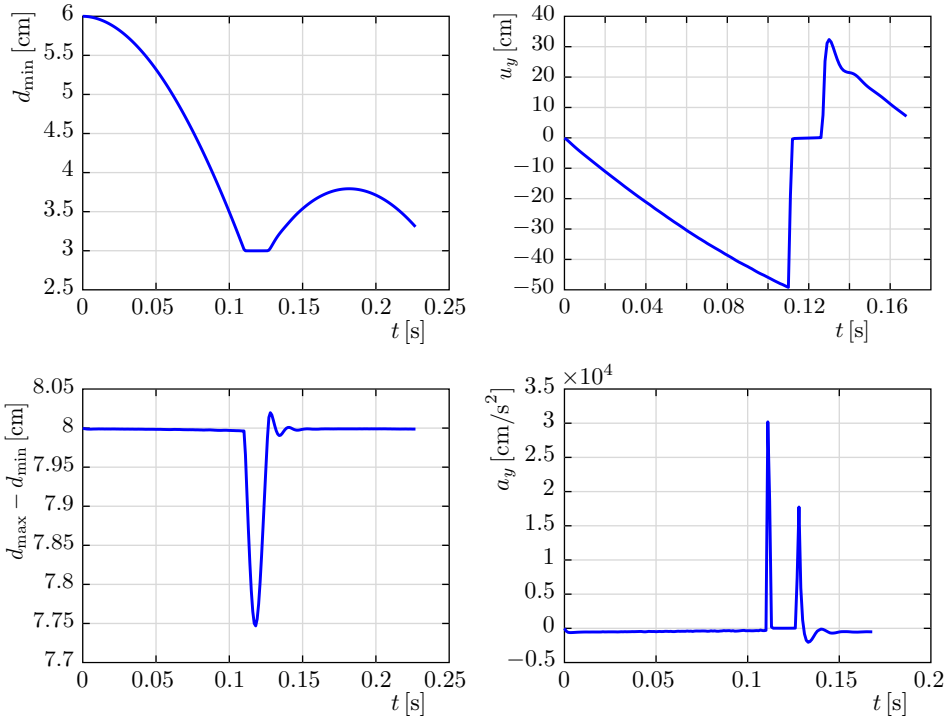

Figure 11. Top-left: minimum distance from Γ^w of the ball over time. Bottom-left: compression of the ball over time. Top-right: velocity over time of the solid point at the minimum distance from Γ^w. Bottom-right: acceleration over time of the solid point at minimum distance from Γ^w. "Virtual barrier" test case.

4.3. Contact of an elastic ball with a rigid ground. In this examples, we consider the configuration and parameters used for the test in Section 4.2. The difference is that we set $\varepsilon = h$ to model the contact with the rigid ground.

In Figure 12, we plot the evolution in time of the minimum distance $d_{\min}$ (top-left, top-right), the velocity u_y (bottom-left), and the compression $d_{\max} - d_{\min}$ of the ball (bottom-right). We notice that, differently from the case of the virtual barrier, in this case when the ball approaches Γ^w, it is already compressed due to the high fluid pressure generated by the presence of Γ^w.

In Figure 13, we plot the vorticity isolines and fluid velocity vectors at $t = 0.177\,\mathrm{s}$, i.e. when the ball comes into contact with the ground.

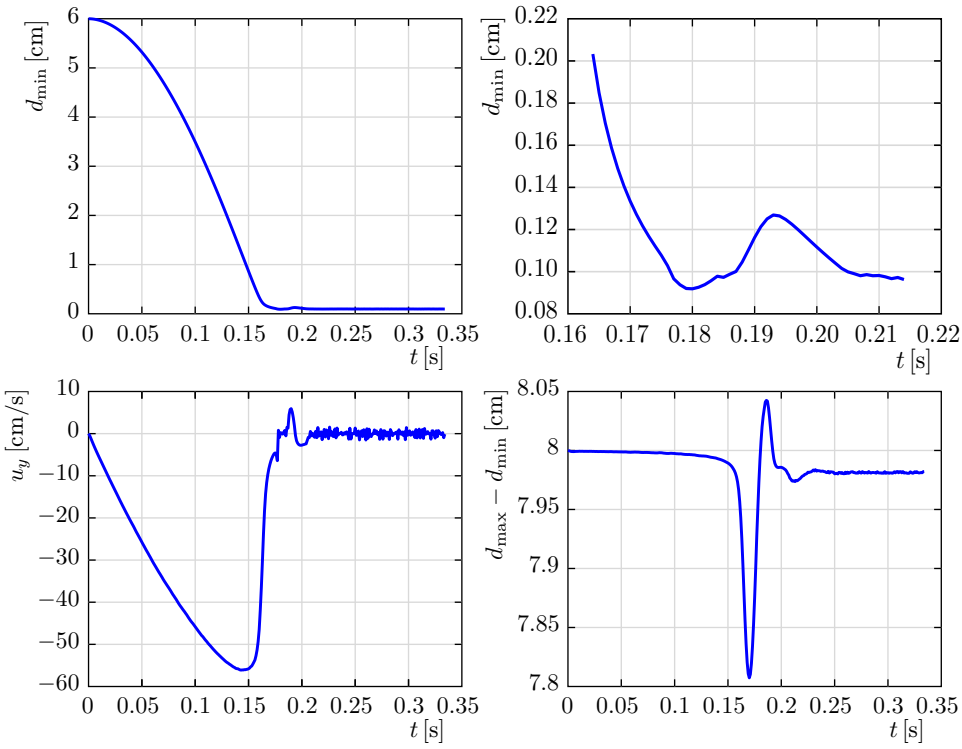

Figure 12. Top-left: minimum distance from Γ^w of the ball over time. Top-right: zoom of the minimum distance during the contact phase. Bottom-left: velocity over time of the ball at the point at the minimum distance from Γ^w. Bottom-right: compression of the ball over time. Results for time step $\Delta t = 10^{-3}$ s. "Rigid ground" test case.

	$\Delta t = 2 \cdot 10^{-3}$ s	$\Delta t = 10^{-3}$ s	$\Delta t = 2 \cdot 10^{-4}$ s
Contact time [s]	0.176	0.177	0.1904
Maximum height [cm]	0.122	0.127	0.153
Maximum height time [s]	0.192	0.193	0.2072

Table 2. Contact time, the maximum height reached by the ball after the rebound and the corresponding time for three different time steps. "Rigid ground" test case.

To investigate the influence of the time step, we perform two simulations with a different value of Δt, namely $2 \cdot 10^{-3}$ s and $2 \cdot 10^{-4}$ s. Table 2 shows the time at which the contact happens (first row of the table), the maximum elevation reached by the ball after the rebound (second row of the table) and the corresponding time (third row of the table), for the three time steps. We observe that the times increase by refining the time step. For the larger time step, i.e. $\Delta t = 2 \cdot 10^{-3}$ s, we have noticed that the ball drops out of the fluid domain at the second bouncing with

the rigid ground. This means that the time step is not sufficiently fine to resolve correctly the contact dynamics. Moreover, we see that the maximum height reached after the rebound increases slightly, as time step decreases: from the greater to the finer time step, the maximum height increases of about 50% of the resolution grid in that region.

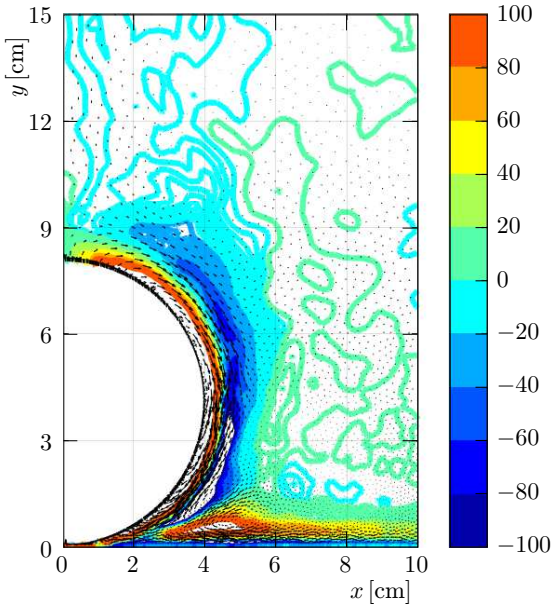

Figure 13. Vorticity isolines and fluid velocity vectors at the instant of contact $t = 0.177\,\mathrm{s}$. Results for time step $\Delta t = 10^{-3}\,\mathrm{s}$. "Rigid ground" test case.

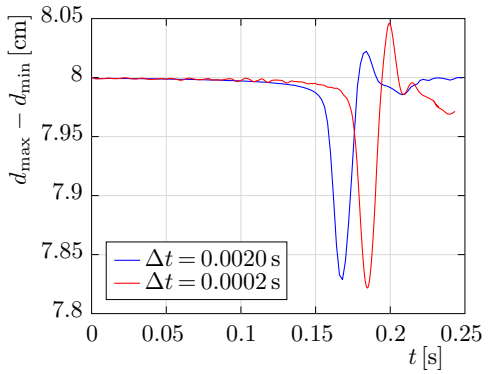

Figure 14. Comparison of the compression between the case $\Delta t = 2 \cdot 10^{-3}\,\mathrm{s}$ and $\Delta t = 2 \cdot 10^{-4}\,\mathrm{s}$. "Rigid ground" test case.

In Figure 14, we show the compression $d_{\max} - d_{\min}$ for the smaller and larger time step. We notice that, for the finer time step, the peaks are delayed in time with

a greater magnitude and the solution exhibits some oscillations before the contact. In Figure 15, we plot the fluid velocity field and the vorticity isolines just after the contact for the case $\Delta t = 2 \cdot 10^{-3}$ s and for the case $\Delta t = 2 \cdot 10^{-4}$ s.

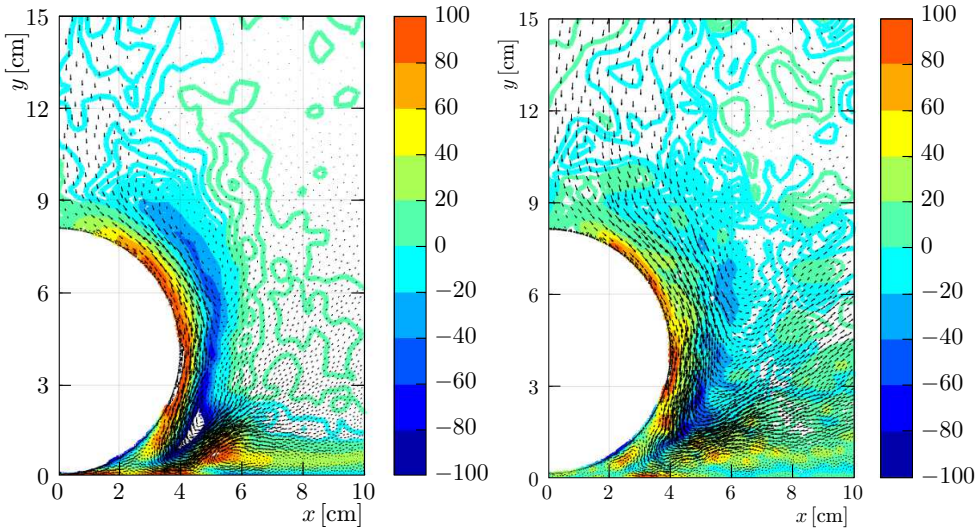

Figure 15. Vorticity and velocity field just after the contact. Top: results for $\Delta t = 2 \cdot 10^{-3}$ s. Bottom: results for $\Delta t = 2 \cdot 10^{-4}$ s. "Rigid ground" test case.

We point out that this test is the same as the one presented in [56]. Notice that to reduce the difference in the orders of magnitude between the values of the physical parameters used in [56], we have applied a scaling to these quantities by introducing a similarity coefficient $K_{\text{sim}} = \frac{1}{10}$. By denoting by $\cdot^*$ the quantities defined in [56], our quantities are scaled as:

$$L = K_{\text{sim}} L^*, \quad T = K_{\text{sim}} T^*, \quad \mathbf{g} = \frac{\mathbf{g}^*}{K_{\text{sim}}},$$

where L and T represent the spatial and temporal scales, respectively, and $\mathbf{g}$ is the acceleration appearing in $\hat{\mathbf{f}}^s$.

Comparing the results that we obtain with the ones shown in [56], we get a very similar contact time. Regarding the maximum height of the ball after the bounce, we see that in our case it is one order of magnitude smaller. However, we have considered a coarser mesh ($h = 0.1$ cm in our case, $h = 0.031$ cm in [56]) and, as shown in [56], the mesh size has a significant effect on the bounce of the ball.

4.4. Contact of an elastic ball with a flexible ground. In this test, we consider a similar configuration to the one used in the test in Section 4.2. The two major differences are that the ground is now elastic, governed by the constitutive

law (2.4) with the same elastic parameters of the ball, and that the initial position of the ball is closer to the ground. In particular, we have a flexible master domain $\widehat{\Omega}^m$ of size $20\,\text{cm} \times 2\,\text{cm}$ with the bottom left corner placed in $(-10, 0)$ and the center of the slave domain $\widehat{\Omega}^s$ located at the point $(0, 7)\,\text{cm}$. We denote with $\Omega = (-10, 10)\,\text{cm} \times (0, 15)\,\text{cm}$ the union of the fluid and solid domains. Notice that the initial distance between the master and slave is 1 cm.

As in the previous tests, a body force $\mathbf{f}^s = \varrho^s \cdot (0, -10^3)\,\text{cm/s}^2$ acts on the ball $\Omega^s(t)$. The flexible ground $\Omega^m(t)$ is clamped at the bottom and at the lateral boundaries, while the upper side is free to move. No body-force acts on the master body. Due to the symmetry with respect to the vertical axis, in the numerical simulations we consider only half of the domain, see Figure 16. We use the physical parameters described in Section 4.2, where the Lamé coefficients are the same for the slave and master bodies.

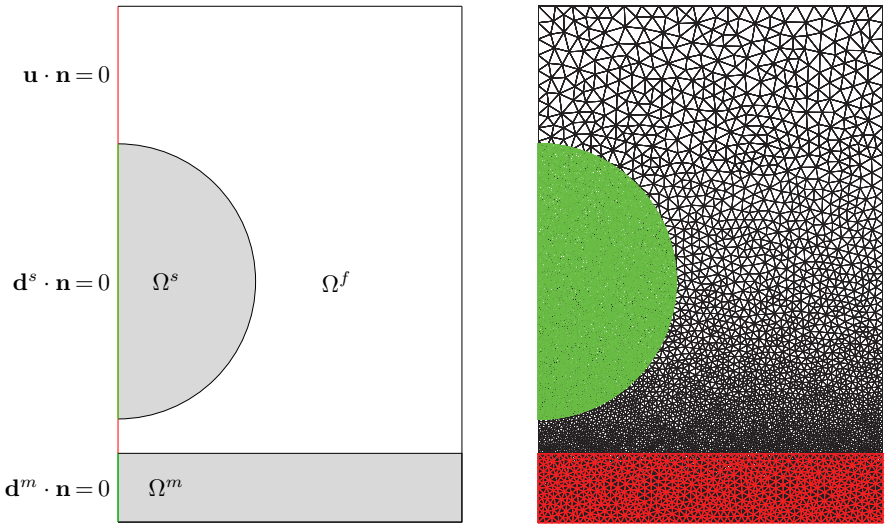

Figure 16. Left: sketch of the reduced domain with the boundary conditions at the symmetry axis (red for the fluid, green for the solids). Right: sketch of the slave body (green) and master one (red). "Flexible ground" test case.

For the background mesh, we use a spatial resolution of about 0.5 cm in the upper part and of 0.05 cm in the lower part. For the slave mesh, we use a space discretization of 0.1 cm, while for the master body of 0.3 cm. We use a time step $\Delta t = 10^{-3}\,\text{s}$. Finally, we set the same penalty parameters as are reported in Section 4.2 and $\varepsilon = h$.

In Figure 17 (left), we show the compression of the ball. As for the case of contact with a rigid ground, the ball slows down before the activation of the contact due to the high fluid pressure. At time 0.081 s the two bodies come into contact. As for the

case of the rigid ground, the ball does not show any further compression at contact but, due to the insufficient internal energy, at time 0.089 s, the ball shows a further compression due to the inability to bounce off the flexible wall. From this point on, the two bodies stay in contact.

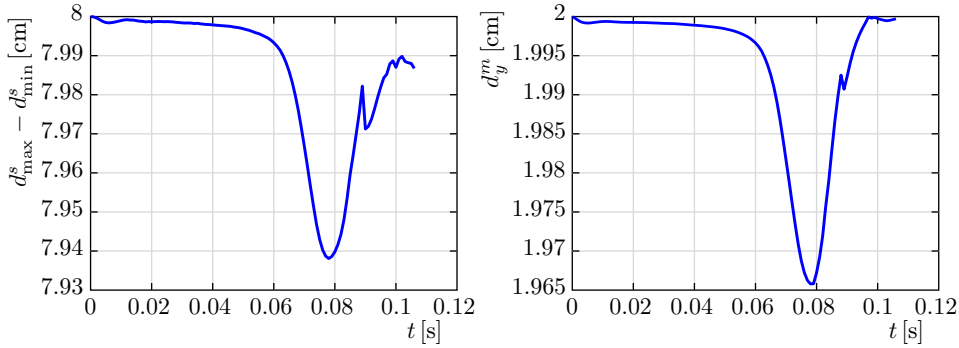

Figure 17. Left: compression of the ball. Right: minimum thickness of the ground. "Flexible ground" test case.

In Figure 18, we plot the displacement isolines at the instant of contact. During contact, the minimum distance between the two bodies is about 50% of the local mesh size.

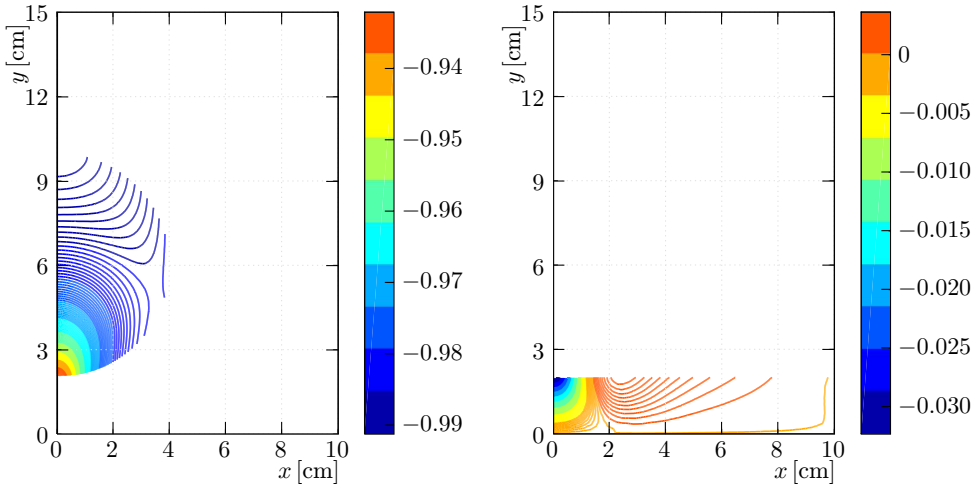

Figure 18. Slave (left) and master (right) vertical displacement isolines at the instant of contact. "Flexible ground" test case.

This example shows how the flexibility of the wall dissipates some of the kinetic and internal energy of the ball, stopping it from bouncing away.

5. Conclusions

In this work, we have proposed a penalization contact method in a XFEM/DG numerical framework for the study of FSI problems with contact in the case of large deformations and large displacements. This approach is relatively easy to implement and is very effective. However, it does not guarantee consistency of the numerical method and the formulation requires the penalty term to be sufficiently high in order to ensure numerical stability, possibly leading to an ill-conditioned matrix. A possible way to overcome these issues is to consider a Nitsche's approach for the contact model. Indeed, it produces a consistent formulation and allows to achieve stability with a lower penalty coefficient, see e.g. [21].

Through the sensitivity analysis, we found that the relaxation parameter ε can be set approximately equal to h. On the contrary, the contact penalty parameter γ_C seems to be more arbitrary and may depend on the considered physical setting. Further studies in this direction are under investigation.

We have shown three examples of increasing geometrical complexity: the contact algorithm performs correctly for the "virtual barrier" test case, although the contact with the rigid and flexible ground test cases present some issues in properly reproducing the bouncing of the ball. In fact, the nature of contact requires to have both a sufficiently high spatial and temporal resolutions to catch the correct behaviour. Moreover, the contact model and the coupling conditions with the fluid on the contact region can be improved to obtain a more physical representation of the phenomena, as proposed in [21] and [1].

Even though the numerical tests are performed on 2D geometrical configurations, the proposed algorithm is suited also for simulating more complex scenarios in 3D.

References

[1] *C. Ager, B. Schott, A.-T. Vuong, A. Popp, W. A. Wall*: A consistent approach for fluid-structure-contact interaction based on a porous flow model for rough surface contact. Int. J. Numer. Methods Eng. *119* (2019), 1345–1378. MR doi

[2] *C. Ager, A. Seitz, W. A. Wall*: A consistent and comprehensive computational approach for general fluid-structure-contact interaction problems. Available at `https://arxiv.org/abs/1905.09744` (2019), 34 pages.

[3] *P. Alart, A. Curnier*: A mixed formulation for frictional contact problems prone to Newton like solution methods. Comput. Methods Appl. Mech. Eng. *92* (1991), 353–375. zbl MR doi

[4] *F. Alauzet, B. Fabrèges, M. A. Fernández, M. Landajuela*: Nitsche-XFEM for the coupling of an incompressible fluid with immersed thin-walled structures. Comput Methods Appl. Mech. Eng. *301* (2016), 300–335. zbl MR doi

[5] *P. Antonietti, M. Verani, C. Vergara, S. Zonca*: Numerical solution of fluid-structure interaction problems by means of a high order Discontinuous Galerkin method on polygonal grids. Finite Elem. Anal. Des. *159* (2019), 1–14. MR doi

[6] *D. N. Arnold, F. Brezzi, B. Cockburn, L. D. Marini*: Unified analysis of discontinuous Galerkin methods for elliptic problems. SIAM J. Numer. Anal. *39* (2002), 1749–1779. zbl MR doi

[7] *F. P. T. Baaijens*: A fictitious domain/mortar element method for fluid-structure interaction. Int. J. Numer. Methods Fluids *35* (2001), 743–761. zbl MR doi
[8] *S. Basting, A. Quaini, S. Čanić, R. Glowinski*: Extended ALE method for fluid-structure interaction problems with large structural displacements. J. Comput. Phys. *331* (2017), 312–336. zbl MR doi
[9] *Y. Bazilevs, V. M. Calo, Y. Zhang, T. J. R. Hughes*: Isogeometric fluid-structure interaction analysis with applications to arterial blood flow. Comput. Mech. *38* (2006), 310–322. zbl doi
[10] *Y. Bazilevs, M.-C. Hsu, J. Kiendl, R. Wüchner, K.-U. Bletzinger*: 3D simulation of wind turbine rotors at full scale II. Fluid-structure interaction modeling with composite blades. Int. J. Numer. Methods Fluids *65* (2011), 236–253. zbl doi
[11] *T. Belytschko, N. Moës, S. Usui, C. Parimi*: Arbitrary discontinuities in finite elements. Int. J. Numer. Methods Eng. *50* (2001), 993–1013. zbl doi
[12] *D. Boffi, L. Gastaldi*: A finite element approach for the immersed boundary method. Comput. Struct. *81* (2003), 491–501. MR doi
[13] *D. Boffi, L. Gastaldi*: A fictitious domain approach with Lagrange multiplier for fluid-structure interactions. Numer. Math. *135* (2017), 711–732. zbl MR doi
[14] *D. Boffi, L. Gastaldi, L. Heltai*: Numerical stability of the finite element immersed boundary method. Math. Models Methods Appl. Sci. *17* (2007), 1479–1505. zbl MR doi
[15] *I. Borazjani*: Fluid-structure interaction, immersed boundary-finite element method simulations of bio-prosthetic heart valves. Comput. Methods Appl. Mech. Eng. *257* (2013), 103–116. zbl MR doi
[16] *I. Borazjani, L. Ge, F. Sotiropoulos*: Curvilinear immersed boundary method for simulating fluid structure interaction with complex 3D rigid bodies. J. Comput. Phys. *227* (2008), 7587–7620. zbl MR doi
[17] *E. Burman*: Ghost penalty. C. R., Math., Acad. Sci. Paris *348* (2010), 1217–1220. zbl MR doi
[18] *E. Burman, M. A. Fernández*: Stabilized explicit coupling for fluid-structure interaction using Nitsche's method. C. R., Math., Acad. Sci. Paris *345* (2007), 467–472. zbl MR doi
[19] *E. Burman, M. A. Fernández*: Stabilization of explicit coupling in fluid-structure interaction involving fluid incompressibility. Comput. Methods Appl. Mech. Eng. *198* (2009), 766–784. zbl MR doi
[20] *E. Burman, M. A. Fernández*: An unfitted Nitsche method for incompressible fluid-structure interaction using overlapping meshes. Comput. Methods Appl. Mech. Eng. *279* (2014), 497–514. zbl MR doi
[21] *E. Burman, M. A. Fernández, S. Frei*: A Nitsche-based formulation for fluid-structure interactions with contact. ESAIM, Math. Model. Numer. Anal. *54* (2020), 531–564. zbl MR doi
[22] *E. Burman, M. A. Fernández, P. Hansbo*: Continuous interior penalty finite element method for Oseen's equations. SIAM J. Numer. Anal. *44* (2006), 1248–1274. zbl MR doi
[23] *E. Burman, P. Hansbo, M. G. Larson*: Augmented Lagrangian and Galerkin least-squares methods for membrane contact. Int. J. Numer. Methods Eng. *114* (2018), 1179–1191. MR doi
[24] *E. Burman, P. Hansbo, M. G. Larson*: Augmented Lagrangian finite element methods for contact problems. ESAIM, Math. Model. Numer. Anal. *53* (2019), 173–195. zbl MR doi
[25] *F. Chouly, M. Fabre, P. Hild, R. Mlika, J. Pousin, Y. Renard*: An overview of recent results on Nitsche's method for contact problems. Geometrically Unfitted Finite Element Methods and Applications. Lecture Notes in Computational Science and Engineering 121. Springer, Cham, 2017, pp. 93–141. zbl MR doi
[26] *F. Chouly, P. Hild*: A Nitsche-based method for unilateral contact problems: Numerical analysis. SIAM J. Numer. Anal. *51* (2013), 1295–1307. zbl MR doi
[27] *F. Chouly, P. Hild*: On convergence of the penalty method for unilateral contact problems. Appl. Numer. Math. *65* (2013), 27–40. zbl MR doi

[28] *F. Chouly, R. Mlika, Y. Renard*: An unbiased Nitsche's approximation of the frictional contact between two elastic structures. Numer. Math. *139* (2018), 593–631. zbl MR doi
[29] *F. Chouly, Y. Renard*: Explicit Verlet time-integration for a Nitsche-based approximation of elastodynamic contact problems. Adv. Model. Simul. Eng. Sci. *5* (2018), Article ID 31, 38 pages. doi
[30] *J. Donea, S. Giuliani, J. P. Halleux*: An arbitrary Lagrangian-Eulerian finite element method for transient dynamic fluid-structure interactions. Comput. Methods Appl. Mech. Eng. *33* (1982), 689–723. zbl doi
[31] *C. Farhat, M. Lesoinne, P. Le Tallec*: Load and motion transfer algorithms for fluid/structure interaction problems with non-matching discrete interfaces: Momentum and energy conservation, optimal discretization and application to aeroelasticity. Comput. Methods App. Mech. Eng. *157* (1998), 95–114. zbl MR doi
[32] *L. Formaggia, F. Nobile*: A stability analysis for the arbitrary Lagrangian Eulerian formulation with finite elements. East-West J. Numer. Math. *7* (1999), 105–131. zbl MR
[33] *L. Formaggia, C. Vergara, S. Zonca*: Unfitted extended finite elements for composite grids. Comput. Math. Appl. *76* (2018), 893–904. zbl MR doi
[34] *S. Frei*: Eulerian Finite Element Methods for Interface Problems and Fluid-Structure Interactions: PhD. Thesis. Heidelberg University, Heildelberg, 2016. doi
[35] *S. Frei, T. Richter, T. Wick*: Long-term simulation of large deformation, mechano-chemical fluid-structure interactions in ALE and fully Eulerian coordinates. J. Comput. Phys. *321* (2016), 874–891. zbl MR doi
[36] *A. Gerstenberger, W. A. Wall*: An eXtended Finite Element Method/Lagrange multiplier based approach for fluid-structure interaction. Comput. Methods Appl. Mech. Eng. *197* (2008), 1699–1714. zbl MR doi
[37] *R. Glowinski, T.-W. Pan, J. Periaux*: A fictitious domain method for Dirichlet problem and applications. Comput. Methods Appl. Mech. Eng. *111* (1994), 283–303. zbl MR doi
[38] *B. E. Griffith*: Immersed boundary model of aortic heart valve dynamics with physiological driving and loading conditions. Int. J. Numer. Methods Biomed. Eng. *28* (2012), 317–345. zbl MR doi
[39] *A. Hansbo, P. Hansbo*: A finite element method for the simulation of strong and weak discontinuities in solid mechanics. Comput. Methods Appl. Mech. Eng. *193* (2004), 3523–3540. zbl MR doi
[40] *P. Hansbo, J. Hermansson, T. Svedberg*: Nitsche's method combined with space-time finite elements for ALE fluid-structure interaction problems. Comput. Methods Appl. Mech. Eng. *193* (2004), 4195–4206. zbl MR doi
[41] *C. W. Hirt, A. A. Amsden, J. L. Cook*: An arbitrary Lagrangian-Eulerian computing method for all flow speeds. J. Comput. Phys. *14* (1974), 227–253. zbl doi
[42] *N. Kikuchi, J. T. Oden*: Contact Problems in Elasticity: A Study of Variational Inequalities and Finite Element Methods. SIAM Studies in Applied Mathematics 8. Society for Industrial and Applied Mathematics, Philadelphia, 1988. zbl MR doi
[43] *LifeV*: Available at `https://bitbucket.org/lifev-dev/lifev-release/wiki/Home`. sw
[44] *Y. Liu, W. K. Liu*: Rheology of red blood cell aggregation by computer simulation. J. Comput. Phys. *220* (2006), 139–154. zbl MR doi
[45] *G. Marom*: Numerical methods for fluid-structure interaction models of aortic valves. Arch. Comput. Methods Eng. *22* (2015), 595–620. zbl MR doi
[46] *A. Massing, M. G. Larson, A. Logg, M. E. Rognes*: A Nitsche-based cut finite element method for a fluid-structure interaction problem. Commun. Appl. Math. Comput. Sci. *10* (2015), 97–120. zbl MR doi
[47] *R. Mittal, G. Iaccarino*: Immersed boundary methods. Annu. Rev. Fluid Mech. *37* (2005), 239–261. zbl MR doi

[48] *N. Moës, J. Dolbow, T. Belytschko*: A finite element method for crack growth without remeshing. Int. J. Numer. Methods Eng. *46* (1999), 131–150. zbl MR doi
[49] *E. Oñate, M. A. Celigueta, S. R. Idelsohn, F. Salazar, B. Suárez*: Possibilities of the particle finite element method for fluid-soil-structure interaction problems. Comput. Mech. *48* (2011), 307–318. zbl MR doi
[50] *N. A. Patankar, P. Singh, D. D. Joseph, R. Glowinski, T.-W. Pan*: A new formulation of the distributed Lagrange multiplier/fictitious domain method for particulate flows. Int. J. Multiphase Flow *26* (2000), 1509–1524. zbl doi
[51] *C. S. Peskin*: Flow patterns around heart valves: A numerical method. J. Comput. Phys. *10* (1972), 252–271. zbl doi
[52] *C. S. Peskin*: The immersed boundary method. Acta Numerica *11* (2002), 479–517. zbl MR doi
[53] *R. Rannacher, T. Richter*: An adaptive finite element method for fluid-structure interaction problems based on a fully Eulerian formulation. Fluid Structure Interaction II. Modelling, Simulation, Optimization. Lecture Notes in Computational Science and Engineering 73. Springer, Berlin, 2010, pp. 159–191. zbl MR doi
[54] *G. Rega*: Nonlinear vibrations of suspended cables I. Modeling and analysis. Appl. Mech. Rev. *57* (2004), 443–478. doi
[55] *T. Richter*: A fully Eulerian formulation for fluid-structure-interaction problems. J. Comput. Phys. *233* (2013), 227–240. MR doi
[56] *T. Richter*: Fluid-Structure Interactions: Models, Analysis and Finite Elements. Lecture Notes in Computational Science and Engineering 118. Springer, Cham, 2017. zbl MR doi
[57] *T. Richter, T. Wick*: Finite elements for fluid-structure interaction in ALE and fully Eulerian coordinates. Comput. Methods Appl. Mech. Eng. *199* (2010), 2633–2642. zbl MR doi
[58] *P. H. Saksono, W. G. Dettmer, D. Perić*: An adaptive remeshing strategy for flows with moving boundaries and fluid-structure interaction. Int. J. Numer. Methods Eng. *71* (2007), 1009–1050. zbl MR doi
[59] *C. Vergara, S. Zonca*: Extended finite elements method for fluid-structure interaction with an immersed thick non-linear structure. Mathematical and Numerical Modeling of the Cardiovascular System and Applications. SEMA SIMAI Springer Series 16. Springer, Cham, 2018, pp. 209–243. MR doi
[60] *P. Wriggers, G. Zavarise*: Computational contact mechanics. Encyclopedia of Computational Mechanics II. Solids and Structures. John Wiley & Sons, Chichester, 2004, Article ID 6. doi
[61] *D. Xu, E. Kaliviotis, A. Munjiza, E. Avital, C. Ji, J. Williams*: Large scale simulation of red blood cell aggregation in shear flows. J. Biomech. *46* (2013), 1810–1817. doi
[62] *H. Zhang, L. Liu, M. Dong, H. Sun*: Analysis of wind-induced vibration of fluid-structure interaction system for isolated aqueduct bridge. Eng. Struct. *46* (2013), 28–37. doi
[63] *S. Zonca*: Unfitted Numerical Methods for Fluid-Structure Interaction Arising Between an Incompressible Fluid and an Immersed Thick Structure: PhD. Thesis. Politecnico di Milano, Milano, 2018.
[64] *S. Zonca, C. Vergara, L. Formaggia*: An unfitted formulation for the interaction of an incompressible fluid with a thick structure via an XFEM/DG approach. SIAM J. Sci. Comput. *40* (2018), B59–B84. zbl MR doi

Authors' address: *Luca Formaggia* (corresponding author), *Federico Gatti*, *Stefano Zonca*, Dipartimento di Matematica, Modellistica e calcolo scientifico (MOX), Politecnico di Milano, Piazza Leonardo da Vinci 32, 20133 Milano, Italy, e-mail: `luca.formaggia@polimi.it`, `federico.gatti@polimi.it`, `stefano.zonca@polimi.it`.